Electrochimica Acta 574 (2026) 149379

Contents lists available at ScienceDirect

Electrochimica Acta

journal homepage: www.journals.elsevier.com/electrochimica-acta

Recirculating carbonate and bicarbonate based electrolyzers cannot operate continuously without in-line separation due to electrolyte depletion and ion crossover

Sohan A. Phadke *, J.W. Haverkort, Wiebren de Jong

Process & Energy Department, Mechanical Engineering, Delft University of Technology, Leeghwaterstraat 39, Delft, 2628CB, Zuid-Holland, Netherlands

ARTICLE INFO

Keywords:
Electrolyte depletion
Ion transport
Water electrolysis
Dissolved carbon loss
Multiphysics model

ABSTRACT

The commercialization of (bi)carbonate-based electrolyzers for reactions such as CO_2 reduction requires examination of their long-term operation. We studied the effects of electrolyte depletion and electrolyzer performance drop-off through experiments and simulations in a system with separated, recirculating electrolyte reservoirs. The effects of mass transport, electrochemical reactions, and equilibrium reactions form a combined picture that explains the behavior in these systems, which is characterized by insufficient OH^- transport for electrochemical reactions at the anode surface. The carbonate equilibrium shifts towards bicarbonate as OH^- anions are consumed at the anode, and the bicarbonate equilibrium shifts further to CO_2 as physical gas stripping by O_2 bubbles removes dissolved CO_2 until the electrolyte is fully depleted. We reduce the system into a simplified 1-D numerical model that identifies the relevant phenomena of the system. We use this model in tandem with experiments to show the loss of dissolved carbon from the anolyte inventory due to physical gas stripping that transports CO_2 to the atmosphere. We also observe and model electro-osmotic flow that causes net fluid motion from anolyte to catholyte and decreases the diffusion of dissolved carbon species from cathode to anode. The simulations agree with experimental measurements and show that migration is the dominant component of the ionic transport that sustains the current. Our results show that continuous operation of these systems is not possible without some strategy to improve OH^- transport to the anode, such as recombining electrolyte streams after separation, using novel separators, or operating at much lower current densities.

Nomenclature

Table 1 shows the symbols and variables used in this work.

1. Introduction

With more stringent emissions regulations comes the need for more sustainable methods of chemicals production. One of these methods is the electrochemical formation of commodity chemicals through electrolysis using renewable electricity and/or renewable feedstocks [1]. One example would be carbon dioxide (CO_2) reduction to produce methane, ethylene, oxalate, etc [2]. Another example is the electrochemical production of hydrogen peroxide (H_2O_2) in alkaline systems, which could displace the currently unsustainable production route through anthraquinone oxidation [3,4]. Both of these electrochemical processes, as well as integrated carbon capture and conversion systems, use aqueous electrolytes based on either carbonate (CO_3^{2-}) or bicarbonate (HCO_3^-) as the anion, rather than the typical OH^- based electrolytes used in commercial alkaline water electrolysis [5–8]. But these aqueous, (bi)carbonate-based electrolyzers have some drawbacks. One issue is larger ohmic losses due to the lower conductivity of the electrolyte when compared to the typical 30 wt% potassium hydroxide (KOH) solution used in alkaline water electrolysis [9,10]. Another drawback is that the lower concentration of charge-carrying hydroxide (OH^-) anions compared to 30 wt% KOH means that transport of OH^- from cathode to anode is insufficient to achieve steady-state at high currents [11]. The electrochemical reactions at the anode in (bi)carbonate-based electrolyzers must therefore consume a different source of OH^- anions instead: the electrolyte itself.

The (bi)carbonate anions are part of an equilibrium reaction network involving CO_3^{2-}, HCO_3^-, and CO_2, as well as protons (H^+) and OH^- through water equilibration. Under an applied potential, OH^- anions are consumed at the anode by electrochemical reaction and the local pH drops. Le Chatelier's principle dictates that these equilibrium reactions then shift to provide more free OH^-, which is further consumed by

* Corresponding author.
E-mail address: s.a.phadke@tudelft.nl (S.A. Phadke).

https://doi.org/10.1016/j.electacta.2026.149379
Received 16 March 2026; Received in revised form 19 June 2026; Accepted 21 June 2026
Available online 27 June 2026

Table 1
List of symbols used in this work.

Symbol	Parameter	Units
$N_{D,i}$	Diffusive flux of species i	mol m^{-2} s^{-1}
$D_{Eff,i}$	Effective diffusion coefficient of species i in H_2O	m^2 s^{-1}
$N_{M,i}$	Migratory flux of species i	mol m^{-2} s^{-1}
z_i	Ionic charge of species i	–
μ_i	Electrical mobility	m^2 V^{-1} s^{-1}
F	Faraday's constant	C mol^{-1}
c_i	Concentration of species i in the separator	mol m^{-3}
$\nabla\phi$	Gradient in electrolyte potential	V m^{-1}
$N_{C,i}$	Convective flux of species i	mol m^{-2} s^{-1}
u	Electro-osmotic velocity	m s^{-1}
$N_{B,i}$	Boundary flux of species i	mol m^{-2} s^{-1}
$k_{l,mt}$	Mass transfer coefficient from reservoir to electrode	m s^{-1}
$n_{Res,i}$	Amount of species i in the reservoir	mol
$V_{Elec}(t)$	Electrolyte volume of anolyte or catholyte	m^3
A_{Elec}	Geometric electrode area	m^2
r_i	Reaction rate involving species i	mol m^{-3} s^{-1}
j	Current density	A m^{-2}
n	Ratio of electrons per molecule	–
ν_i	Stoichiometric ratio	–
$\mathcal{V}_{m,H_2O}$	Molar volume of water	m^3 mol^{-1}

the anodic reactions. This can equivalently be viewed as arising from the generation of H^+ ions from the anodic reactions. In the catholyte, the OH^- produced at the cathode cannot be transported through the porous separator to the anode quickly enough, and the catholyte pH rises. During this time, both CO_3^{2-} and HCO_3^- are also transported to the anolyte by migration and diffusion, where they undergo the same equilibrium shifts [12,13].

This pH swing can be mitigated in standard alkaline water electrolysis, where the anolyte and catholyte can be recombined after gas separation using a balancing line. The balancing line connects the two electrolyte tanks and ensures continual operation [14]. But in an electrochemical system that produces liquid products like H_2O_2 instead of exclusively gaseous products, the reservoirs cannot be mixed, as doing so would introduce the liquid product to the opposite electrode reaction and decompose it. Re-mixing the electrolyte would require in-line separation, which is very difficult for the low single-pass product concentrations that are typically achieved with these devices. When the electrolyte is recirculated in these systems without re-mixing, the OH^- capacity in the anolyte steadily depletes, and the pH difference between the two chambers increases [15–17]. As this continues, the current drops to a limiting value as the electrode reactions slow down. Due to this equilibrium-based OH^- capacity of the electrolyte, the reaction can run for longer than compared to dilute KOH solution of the same pH, but the depletion will still inevitably occur. This unsteady operation is detrimental to commercial chemicals production by electrolysis, as lower current leads to lower chemical production rates. Therefore, the phenomenon of electrolyte depletion must be better understood if we hope to industrialize these processes.

Previous investigations into the topic have either focused mainly on the crossover of CO_2 reduction products from catholyte to anolyte, the impact of reaction conditions on product selectivity, or the migration of dissolved carbon species when CO_2 is being fed from the cathode side [17–21]. Here, we present experiments showing electrolyte depletion in a zero-gap alkaline water electrolyzer using carbonate-based electrolyte and recirculating flow with separated reservoirs. Our experiments do not include a pressurized feed of CO_2 into the catholyte through a gas-diffusion electrode, meaning that we are examining a system without an additional influx of species that lowers the overall pH. We also perform simulations using COMSOL Multiphysics to explore the system dynamics and identify key processes that explain the observed behavior. The results show that CO_3^{2-} is depleted in the anolyte by the electrochemical demand of the anodic reactions, but that HCO_3^- is then depleted due to physical gas stripping of CO_2 from solution by the generated O_2 bubbles. This results in a significant amount of dissolved carbon loss, as dissolved carbon species also migrate across the separator to the anode, where they are then equilibrated away to gaseous CO_2. We found that the migration of anionic species was the most significant contributor to the observed current until just before the electrolyte is fully depleted. The results also provided secondary evidence for the reaction mechanism of anodic H_2O_2 formation based on the peroxydicarbonate ($C_2O_6^{2-}$) catalytic pathway.

2. Methods

2.1. Experimental setup

We constructed a zero-gap electrolyzer using laser-cut sheets of 5 mm thick poly(methyl methacrylate) (PMMA) and gaskets of silicone and ethylene propylene diene monomer (EPDM) rubber. An image of the electrolyzer can be seen in Fig. 1. The cell was compressed together using nuts and bolts and made leak-tight with the aid of a thin, 3-D printed insert that added extra compressive force around the electrode chambers and prevented undesired crossover around the separator. Hose pillars were 3-D printed using Formlabs V4 resin and epoxied into the PMMA endplates. The electrolyte used was 1 M Na_2CO_3 (Merck, ACS Reagent, anhydrous, ≥99.5%, granules) made using milli-Q water (Merck Millipore, 18.2 MΩ cm). The separator used was Zirfon Perl UTP 500 from Agfa (500 μm thickness, 50% porosity). The separator was kept submerged in the 1 M Na_2CO_3 electrolyte between experiments in order to keep it hydrated and retain its transport properties. The anode used was Boron-Doped Diamond (BDD), 50 cm^2 from Condias, 2500 ppm p-type doping, chemical vapor deposition coated onto both sides of an expanded metal niobium substrate. BDD was chosen due to the need for a stable material under extremely oxidizing conditions. Many anodes were tested, such as nickel, stainless steel, and some proprietary coated electrodes, but all except BDD underwent significant corrosion during the experiments. Even though BDD is known to perform side reactions, detailed later in Section 2.2, priority was given to having a stable anode that avoided the complications of corrosion side reactions. The cathode was a piece of nickel expanded metal from ExpandoMetal, 0.4 mm thick and 60 cm^2. The current collectors were water-jet cut from 1 mm thick titanium plates with vertical busbars spanning the electrode faces. These vertical struts distributed current more evenly across the electrode surface while allowing gas bubbles to escape. These current collectors were glued into a recess that was milled out of the PMMA plates, and they compressed the electrodes onto the separator surface to ensure a zero-gap configuration. To ensure that the only available surface area for ion transport was immediately between the electrodes, a piece of gasket was cut to fit each electrode, which masked off any other separator surface area.

A Delta Elektronika SM15-200D was used to supply power, connected using ring terminals to the current collectors. Two electrolyte reservoirs were constructed from laser-cut PMMA and glued together using Acrifix 0192. During the experiments, these reservoirs were stirred using magnetic stir bars. Experiments were intentionally performed with low volumes of electrolyte (350 mL each for anolyte and catholyte) and large potential differences in order to quickly deplete the electrolyte. With these operating conditions, it was necessary to cool the electrolyte to prevent undesired changes to transport properties or reaction rates due to temperature increase. Simple heat exchangers were constructed using stainless steel Swagelok tubing and placed in a large plastic container that could be filled with ice and water as needed to manually regulate the electrolyte temperature. The electrolyte temperature was maintained between 20 °C and 35 °C, matching literature studies that prefer ambient temperature for improved CO_2 solubility in CO_2 reduction reaction and improved H_2O_2 stability in H_2O_2 electrosynthesis [22–25]. This temperature variation of ±7.5 °C has an effect on the transport properties and reaction rates, and is discussed further in Section 3.1.

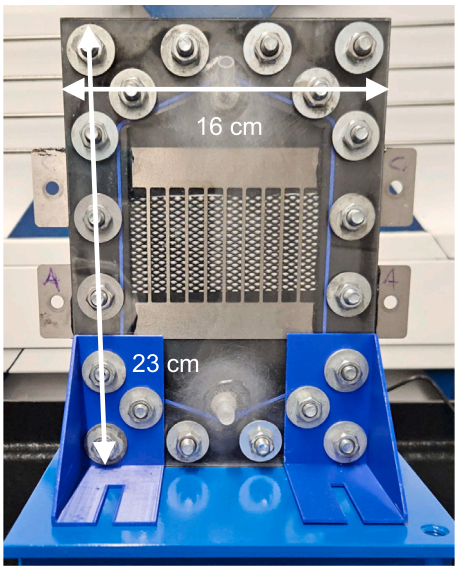

Fig. 1. Photo of the electrolyzer with a view of the anode side. The black BDD expanded metal electrode in the center is surrounded by solid black EPDM gasket of the same thickness, which masks off all porous separator that is not directly in between the electrodes. The single electrode is held in place by the vertical struts of the titanium current collector, which also distribute current evenly across the electrode surface. The tabs extending out the left and right provide terminals for the power supply connections. The thin, blue, diamond-shaped piece around the electrode chamber is the 3-D printed insert that ensures a compressive force around the electrode chambers and prevents any leakage. The entire cell is compressed using nuts and bolts, with 3-D printed feet to keep the electrolyzer upright.

A Longer BT100-3J peristaltic pump with DG15-24 two-channel pump head was used to pump electrolyte through the cell, while keeping the two streams separated. The flow path was from reservoir, through heat exchanger, through one chamber of the electrolyzer, and back to the same reservoir. The flow rate was 250 mL min^{-1}, which led to an electrode chamber residence time of about 15 s. All tubing between components was made from silicone. An image of the full experimental setup is shown in Fig. 2.

During the experiments, a significant electro-osmotic flow from anolyte to catholyte was observed. This change in volume is caused by the negatively charged porous separator inducing a positive counter-charge in the electrolyte, resulting in a net fluid motion [26]. This leads to the anolyte losing water and the catholyte gaining water, contrary to the stoichiometry of the electrochemical reactions. This convective fluid motion makes the concentration gradient less steep and lowers the rate of diffusive flux from cathode to anode, thereby lowering the rate of dissolved carbon species transport and the overall current. The experiments were set to run for 200 min, but were stopped in the case that the anolyte reservoir ran dry and the pump could no longer recirculate electrolyte through the device. With a total of 350 mL of electrolyte on one side, and a volume of 250 mL in the tubing, heat exchanger, and electrode chamber on one side of the device, the current was switched on with 100 mL remaining in the reservoir. If that 100 mL was lost from the anolyte side before 200 min, the experiment was stopped. This restriction prevented salt precipitation issues by keeping the separator submerged throughout.

2.2. Experimental measurement

The power supply was controlled using analog voltage signals provided by a National Instruments Data Acquisition Device. The voltage was fixed at the current collectors to either 7.5 V, 6.5 V, or 5.5 V and

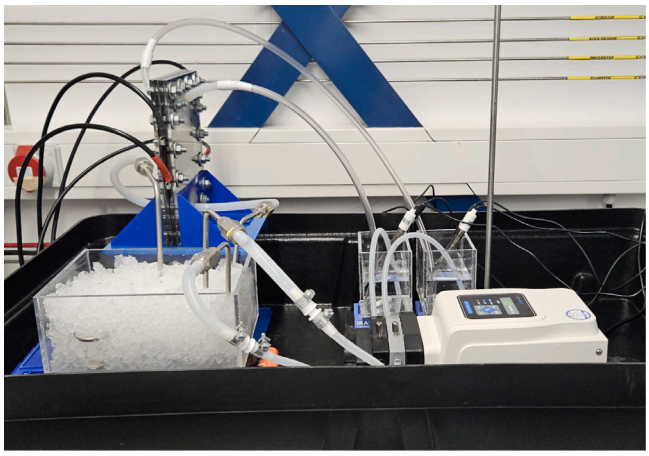

Fig. 2. Photo of the experimental setup. In the bottom right is the peristaltic pump which pumps electrolyte into the heat exchangers in the bottom left. The heat exchangers are stainless steel tubes immersed in a container of ice. The exits of the heat exchangers lead into the electrolyzer in the top left, with black power cables attached to the current collectors. The electrolyte flows into the bottom of each electrode chamber, out the top, and returns to the reservoirs behind the peristaltic pump. Each reservoir has a temperature and pH probe submerged in it.

the current was measured every 0.5 s. The pH and temperature of the reservoirs were monitored using PCE Instruments pH and temperature probes (PCE-228), recording data every 10 s. Experiments started with measured volumes of electrolyte in each reservoir and stopped when the anolyte reservoir ran dry due to electro-osmotic flow bringing electrolyte from anode side to cathode side. This corresponded to a loss of roughly 100 mL, leaving 250 mL remaining to fill the rest of the anolyte side of the system.

The BDD anode used in this experiment has been shown in literature to form peroxydicarbonate ($C_2O_6^{2-}$) through the oxidation of CO_3^{2-} anions [27–29]. The resulting $C_2O_6^{2-}$ is proposed to react with water in the bulk to form H_2O_2 [30]. To measure the produced H_2O_2, we used the potassium permanganate ($KMnO_4$) titration procedure outlined by Gill and Zheng [31]. Briefly, a sample of electrolyte is acidified with a 1:5 diluted sulfuric acid (H_2SO_4, Merck, ACS Reagent, 95%–98%) solution, and then titrated drop-wise using a burette with purple 2 mM $KMnO_4$ solution (Merck, Titripur, standardized against oxalate, 0.02 M, diluted tenfold using milli-Q water) until a light pink color remained in the initially colorless H_2O_2 sample. The volume of $KMnO_4$ added to reach the titration endpoint is then used to calculate the H_2O_2 concentration of the sample based on the stoichiometry.

To measure liberated CO_2 gas from the anolyte, we used a gravimetric assay. The outlet of the anolyte was connected to a simple gas–liquid separator, and when the separated liquid stream flowed into the reservoir, the gas stream was fed into a beaker containing a mixture of 1 M barium chloride ($BaCl_2$ dihydrate, Merck, ACS reagent, ≥99%) solution mixed with 1 M sodium hydroxide (NaOH, Merck, ACS reagent, ≥97%, pellets) solution. This high pH solution readily captured any gaseous CO_2 while letting oxygen bubble through freely. The trapped CO_2, in the form of CO_3^{2-} in solution, then quickly reacted with barium ions in solution to precipitate as the highly insoluble barium carbonate ($BaCO_3$). This precipitate was allowed to settle, vacuum filtered, and then dried in an oven to measure its mass.

2.3. Numerical model development

The model created was a simplified 1-D model using COMSOL Multiphysics v6.2, where the 1-D domain represented the porous separator. The domain was modeled using the "Tertiary Current Distribution,

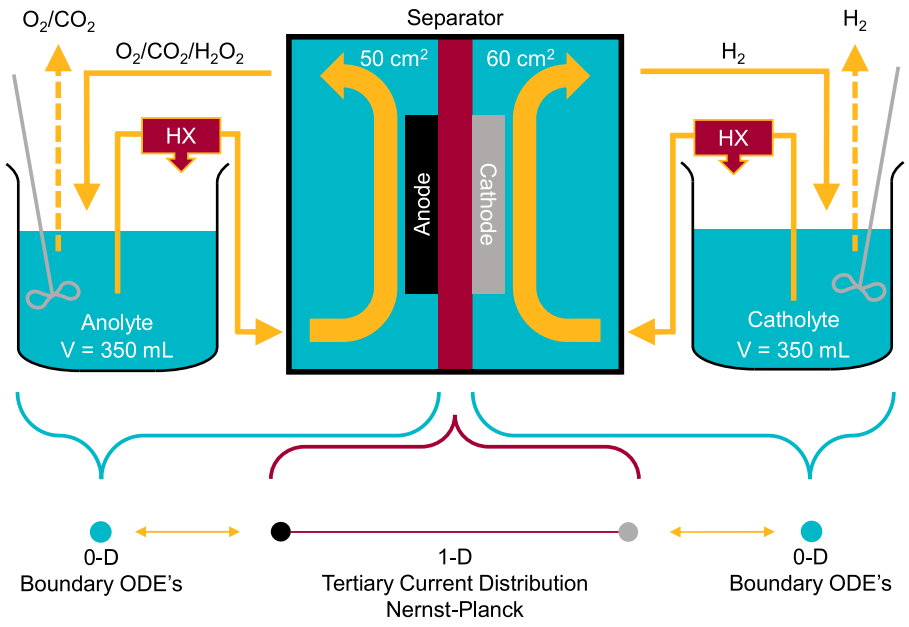

Fig. 3. Schematic of the experimental setup compared to the numerical geometry. The porous separator is treated as a 1-D line segment with the anode and cathode included within the domain. All the electrolyte on one side of the separator (in the reservoir, tubing, heat exchanger, and electrolyzer chamber) is combined into a single set of Boundary ODE's for that side. The HX represents a heat exchanger removing heat from the electrolyte flow before entering the electrode chamber. The solid yellow arrows in the experimental schematic represent electrolyte flow and are represented in the numerical schematic by solid yellow arrows between the 0-D and 1-D domains that are mathematically described using the vertical liquid velocity in the electrode chamber.

Nernst–Planck" interface, with boundary Ordinary Differential Equations (ODE's) used to describe the content of the reservoirs. A schematic showing the experimental setup and its translation to the numerical geometry is depicted in Fig. 3. Whereas other models for such a system are 2-D and include a CO_2 feed through a gas-diffusion electrode, our model can be simplified due to the simpler nature of the transport phenomena near the electrode surfaces [32,33]. Our model includes the contributions of diffusion, migration, and convection, and also enforces electroneutrality everywhere. The effects of temperature change were not included, and the simulation temperature was set to a constant 298.15 K. The full details of the simulation as well as the model file itself can be found in the Supplementary Materials.

The equations satisfied by the model are written in Eqs. (1)–(4).

$$N_{D,i} = -D_{Eff,i}\nabla c_i \tag{1}$$

$$N_{M,i} = -z_i \mu_i F c_i \nabla \phi \tag{2}$$

$$N_{C,i} = u c_i \tag{3}$$

$$\sum z_i c_i = 0 \tag{4}$$

In the above equations, $N_{D,i}$, $N_{M,i}$, and $N_{C,i}$ are the diffusive, migratory, and convective fluxes of species i, respectively, $D_{Eff,i}$ is the effective diffusivity, ∇c_i is the concentration gradient, z_i is the ionic charge, μ_i is the mobility calculated by the Nernst–Einstein relation shown in Equation S16, F is Faraday's constant, and $\nabla\phi$ is the electrolyte potential gradient. The electro-osmotic velocity, u, is calculated based on the electrolyte potential difference and shown in Equations S17 and S18.

The molecular and ionic species included in the simulation were H^+, OH^-, CO_3^{2-}, HCO_3^-, CO_2, $C_2O_6^{2-}$, H_2O_2, HO_2^-, and Na^+. For the anolyte reservoir boundary ODE's, an additional species representing gas phase CO_2, $CO_2(g)$, was also included. Eq. (4) was satisfied in the 1-D separator by balancing the other ionic species with Na^+ as the counterion.

The left boundary of the 1-D domain represented the BDD anode and here the oxygen evolution reaction (OER), peroxydicarbonate ($C_2O_6^{2-}$) generation reaction, and anodic oxidation of H_2O_2 take place. At the right boundary of the 1-D domain representing nickel, only the hydrogen evolution reaction takes place. While nickel has been reported to perform the CO_2 reduction reaction, this is typically only at near-neutral pH and with electrolyte that has been saturated with CO_2 [34,35]. In our system, the catholyte pH is always greater than 11.75, with a negligible fraction of dissolved CO_2, and we therefore limit the model to only the hydrogen evolution reaction at the cathode. These four electrochemical reactions are detailed in Eqs. (5)–(8). The electrochemical reactions are shown here in their alkaline form, but as the pH of the anolyte drops, the acidic pathway of the reactions may occur. We refer to OH^- as the dominant charge carrier compared to H^+, but the reactions were in fact all modeled in their acidic form, as discussed later in Section 2.3.1. These are physically equivalent to the alkaline form through the water dissociation reaction, which is also modeled.

$$4\,OH^- \rightarrow O_2 + 2\,H_2O + 4\,e^- \tag{5}$$

$$2\,CO_3^{2-} \rightarrow C_2O_6^{2-} + 2\,e^- \tag{6}$$

$$H_2O_2 + 2\,OH^- \rightarrow O_2 + 2\,H_2O + 2\,e^- \tag{7}$$

$$2\,H_2O + 2\,e^- \rightarrow 2\,OH^- + H_2 \tag{8}$$

The electrochemical kinetics were modeled using the Butler–Volmer equation shown in Equation S14, with the equilibrium potential calculated using the Nernst equation shown in Equation S13. To account for concentration overpotential effects, the exchange current density term in the Butler–Volmer equation for the anodic reactions was multiplied by a concentration normalization factor, shown in Table S5.

Each electrode was also modified with a film resistance term in order to account for the ohmic loss over the external circuit and

current collectors. A simple measurement of the current collectors was performed by directly connecting the power supply leads to the center and one outer flap of a single current collector and measuring the ohmic drop. The resulting measurement of 15 mΩ was then fixed as the film resistance on each electrode in the simulation as an approximation of ohmic losses.

The equilibrium reactions mentioned earlier concerning the electrolyte are shown in Eqs. (9)–(11). The unidirectional reactions for the formation and bulk disproportionation of H_2O_2 are shown in Eqs. (12) and (13). Lastly, the equilibrium reaction for the deprotonation of H_2O_2 based on pH is shown in Eq. (14). These reactions occur everywhere in the simulation and details of their implementation can be found in Table S3.

$$CO_2 + OH^- \rightleftharpoons HCO_3^- \tag{9}$$

$$HCO_3^- + OH^- \rightleftharpoons CO_3^{2-} + H_2O \tag{10}$$

$$H_2O \rightleftharpoons OH^- + H^+ \tag{11}$$

$$C_2O_6^{2-} + 2\,H_2O \rightarrow 2\,HCO_3^- + H_2O_2 \tag{12}$$

$$2\,H_2O_2 \rightarrow O_2 + 2\,H_2O \tag{13}$$

$$H_2O_2 + OH^- \rightleftharpoons HO_2^- + H_2O \tag{14}$$

At each end of the 1-D domain, overlapping with the electrodes, a flux boundary condition was imposed in order to exchange contents with the reservoirs, shown in Eq. (15).

$$N_{B,i} = k_{l,\,\mathrm{mt}}\left(\frac{n_{\mathrm{Res},i}}{V_{\mathrm{Elec}}(t)} - c_i\Big|_B\right) - u\frac{n_{\mathrm{Res},i}}{V_{\mathrm{Elec}}(t)} \tag{15}$$

In the expression for the boundary flux of species i, $N_{B,i}$, the first term on the right-hand represents the recirculating flow of electrolyte to the electrode chamber, where $k_{l,\,\mathrm{mt}}$ is the mass transfer coefficient of 8.3 mm s^{-1}, $n_{\mathrm{Res},i}$ is the amount of species i in the reservoir (in moles), $V_{\mathrm{Elec}}(t)$ is the anolyte or catholyte volume as a function of time, and $c_i\big|_B$ is the concentration of species i at the boundary of the 1-D domain representing the separator. The precise value of $k_{l,\,\mathrm{mt}}$ was set equal to the average superficial vertical liquid velocity in the electrode chamber, but is not significant so long as it is large enough. The second term on the right-hand side represents the amount of species transported by electro-osmotic flow from anolyte into the 1-D domain, where u is the electro-osmotic velocity. For the boundary at the cathode, the second term on the right-hand side is replaced by $+uc_i\big|_B$, to account for the contents of the 1-D domain being convected to the catholyte reservoir.

The electrolyte outside of the separator was modeled as a well-stirred vessel of homogeneous concentration using a set of boundary ODE's with the following general form:

$$\frac{dn_{\mathrm{Res},i}}{dt} = -N_{B,i}A_{\mathrm{Elec}} + \left(\sum_i r_i\right)V_{\mathrm{Elec}}(t) \tag{16}$$

Eq. (16) models the change in reservoir species by including the contributions of the flux boundary conditions and the homogeneous reactions mentioned earlier. The first term on the right-hand side is equal and opposite to Eq. (15) multiplied by the geometric electrode surface area, A_{Elec}. The second term on the right-hand side represents the homogeneous reactions that occur at all points in the electrolyte, including the reservoirs and tubing, where $\sum r_i$ is the sum of reaction rate terms involving species i. The equation for $dn_{\mathrm{Res},CO_2}/dt$ in the anolyte includes a term that accounts for physical gas stripping of dissolved CO_2 based on the gas fractions that result from the calculated currents. Conversely, the equation for $dn_{\mathrm{Res},CO_2}/dt$ in the catholyte includes a term for the modest uptake of atmospheric CO_2 into a stirred, alkaline reservoir. These additional terms are detailed in Equations S28 and S29.

The equation for $V_{\mathrm{Elec}}(t)$ is found by solving Eq. (17).

$$\frac{dV_{\mathrm{Elec}}(t)}{dt} = \left(A_{\mathrm{Elec}}\sum_{H_2O}\frac{j}{nF} + V_{\mathrm{Elec}}(t)\sum_{H_2O}\nu_i r_i\right)\mathcal{V}_{m,H_2O} \pm uA_{\mathrm{Elec}} \tag{17}$$

In Eq. (17), the first term on the right-hand side represents the total volume of H_2O that is either generated or consumed through electrochemical and homogeneous reactions, while the second term represents the volume gained or lost due to electro-osmotic flow. Instead of modeling electro-osmotic drag, which require ion-specific coefficients, we instead model the overall electro-osmotic flow, which depends only on an empirical zeta potential. The individual species movement is then calculated using the boundary species concentrations along with the volume change. More details are shown in the Supplementary Information. The symbol j is the individual current density of the electrochemical reaction, n is the molar ratio of electrons to water, ν_i is the stoichiometric ratio of water in the homogeneous reactions, and $\mathcal{V}_{m,H_2O}$ is the molar volume of water at 298.15 K.

2.3.1. Numerical methods

Due to a large range of time scales across the electrochemical kinetics, homogeneous reaction rates, and transport phenomena, the numerical system described above is an extremely stiff system of differential equations. The anode boundary in particular experiences the combined effects of diffusion, migration, convection, electrochemical reactions, homogeneous reactions, and flux conditions, all while OH^- is being slowly depleted. This leads to very steep gradients in concentration and reaction rates near the boundaries. To improve stability, many of the reactions are thus numerically described in terms of producing H^+ rather than consuming OH^-.

The time-dependent simulation uses quadratic element order for species concentration, electric potential, and electrolyte potential in the 1-D domain, and also uses quadratic element order for species amounts in the 0-D domain. The implicit solver was fully coupled, and used undamped Newton's method and adaptive backwards differentiation formula with maximum order 2 and minimum order 1. The mesh across the 1-D domain consisted of three separate meshes. Two of the meshes were fine meshes of 2.5 nm element size for a total of 150 nm each at either end of the 1-D domain, to better capture the steep gradients that occurred. The center of the 1-D domain used larger elements of maximum 2.5 μm, with a distribution gradually reducing the element density from the mesh near the boundaries to the center of the domain. This led to a total of 445 mesh elements. A mesh refinement study showed that decreasing the maximum element size up to a factor of 10 led only to small changes in relative values of current (< 3%) and anolyte pH (< 1%), at the cost of increasing the computational time from minutes to many hours. The mesh refinement study and its details are included in Figures S5a-d.

3. Results and discussion

3.1. Experimental-simulation agreement

The current at constant cell potentials, shown in Fig. 4, began with a sharp increase within the first few minutes. This was likely the result of initial activation of the electrodes due to changes in surface chemistry or oxidation state, or a result of local heating of the device. The cell current then decayed approximately linearly and a significant electro-osmotic flow was observed from anolyte chamber to catholyte chamber. The comparison of the experiments with the numerical model are shown in Fig. 4, with solid lines representing experiments and dashed lines representing simulations. There is overall agreement in

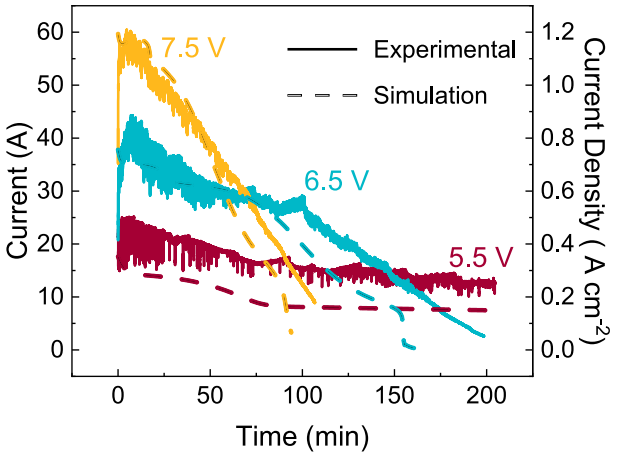

Fig. 4. Plot of current versus time profiles at three constant cell potentials, where solid lines indicate experimental data and dashed lines indicate the simulation values. Experiments and simulations were performed at 1 bar and 25 °C, beginning with 1 M Na_2CO_3. After an initial increase, the currents all decay roughly linearly on different time scales. The fluctuations in the experimental data are due to the fast sampling rate of 0.5 s, and the data shown here has not been smoothed or averaged. The current density is calculated using the geometric anode area of 50 cm^2. The measurement error of the current is ±0.1 A.

shape and magnitude of the profiles with a slight underprediction by the model. A likely source of the discrepancy between the experimental and simulation results at later times is the temperature. Increased temperatures improve transport through the separator and also increase the electrochemical reaction rates. The simulation is run at a constant temperature of 25 °C, and therefore misses some of the temperature dependencies in the experimental system. With slightly increased ionic transport due to initially higher temperatures, we would expect that the time to electrolyte depletion would be slightly delayed, which is consistent with the results shown in Fig. 4. A plot of the reservoir volumes from the simulations is shown in Figure S1.

Through simulations, we can decompose the current and derive the individual contributions. Fig. 5a shows that much of the delivered current is due to migration rather than due to diffusion. We can also decompose the current by reaction type, as in Fig. 5b, which shows for the case of 7.5 V cell potential that while OER and the $C_2O_6^{2-}$ generation reaction are initially of similar order, the latter decreases while the anodic oxidation of H_2O_2 increases. The anodic oxidation of H_2O_2 then decreases until only OER remains. Similar plots for 6.5 V and 5.5 V cell potential can be found in Figures S2a and b.

Examining the experimentally measured pH of the anolyte reservoir over time reveals a quick decay to a value of approximately 8.5, which is roughly the pH of 1 M $NaHCO_3$. This result is in agreement with previously reported results. [19,36,37] Fig. 6a shows the comparison between experimental and simulated results for anolyte pH over time. As cell potential increases, the drop to the lower pH value plateau occurs more quickly. At 7.5 V and 6.5 V, the anolyte pH then slightly increases before dropping again. We do not know the reason for the slight increase, but it may be due to CO_2 gas stripping slightly outpacing the OH^- consumption from electrochemical reactions. The shape of the overall behavior is captured well by the simulations, but the timescales and magnitudes are slightly off. Fig. 6b shows the comparison between experimental and simulated results for catholyte pH over time. Again, the qualitative agreement is correct, while the magnitudes are off. However, this change in magnitude could be due to the pH probe measurement error becoming larger as the pH approaches 14.

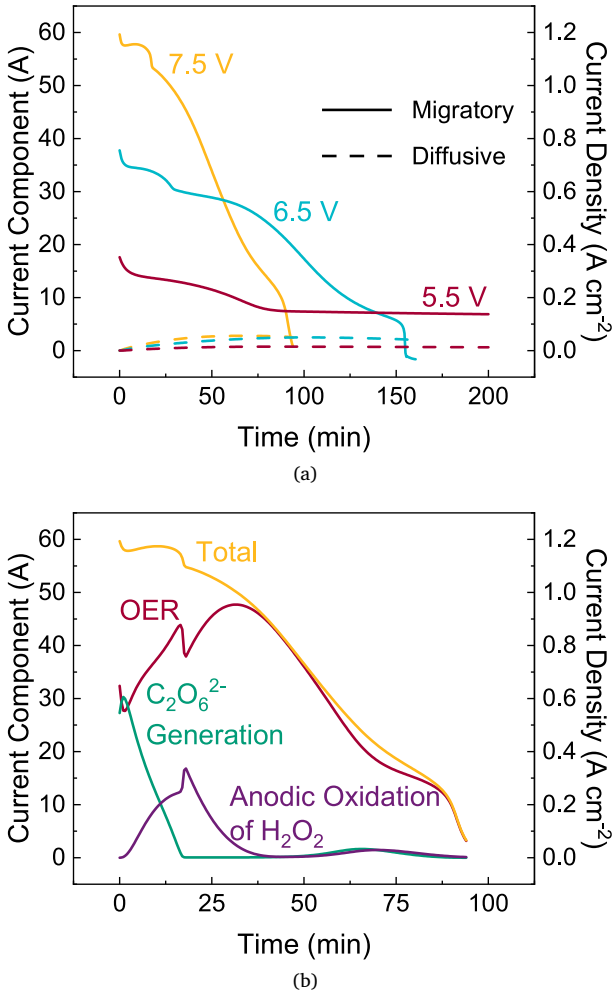

Fig. 5. (a) Plot of the contributions of migration and diffusion to the simulated cell currents at three different cell voltages, for simulations at 1 bar, 298.15 K, and beginning with 1 M Na_2CO_3. Migration is almost always the largest contributor of the current, until the anolyte is fully depleted, at which point diffusion becomes the dominant current contribution. (b) Plot of the simulated current at 7.5 V cell potential, decomposed by electrochemical reaction at the anode for the same starting conditions as in (a).

3.2. Simulation results for electrolyte depletion

The simulation results for ion species concentration across the separator explain how the electrolyte depletes during operation. Fig. 7 shows how the concentrations across the separator evolve over time for the case of 7.5 V. There is initially a sharp decrease in CO_3^{2-} concentration with a corresponding increase in HCO_3^- concentration near the anode. As OH^- is consumed at the anode, the equilibrium of Eq. (10) shifts to provide more OH^- for the electrochemical reactions, producing HCO_3^- with a corresponding drop in anolyte pH during this time. Near the cathode, there is a corresponding increase in OH^- and Na^+ as the produced OH^- cannot transport quickly enough to the anode. As time goes on, the OH^- and Na^+ concentrations continue increasing near the cathode and the HCO_3^- concentration decreases near the anode. The Supplementary Materials include short movies of the relevant species' concentrations as a function of position across the separator over the simulation time, for each of the cell potentials simulated. These videos show the gradual depletion of ions at the anode due to electrochemical reactions exceeding the rate of ion transport across the separator. The effect of this behavior on the reservoir contents can be seen in Fig. 8.

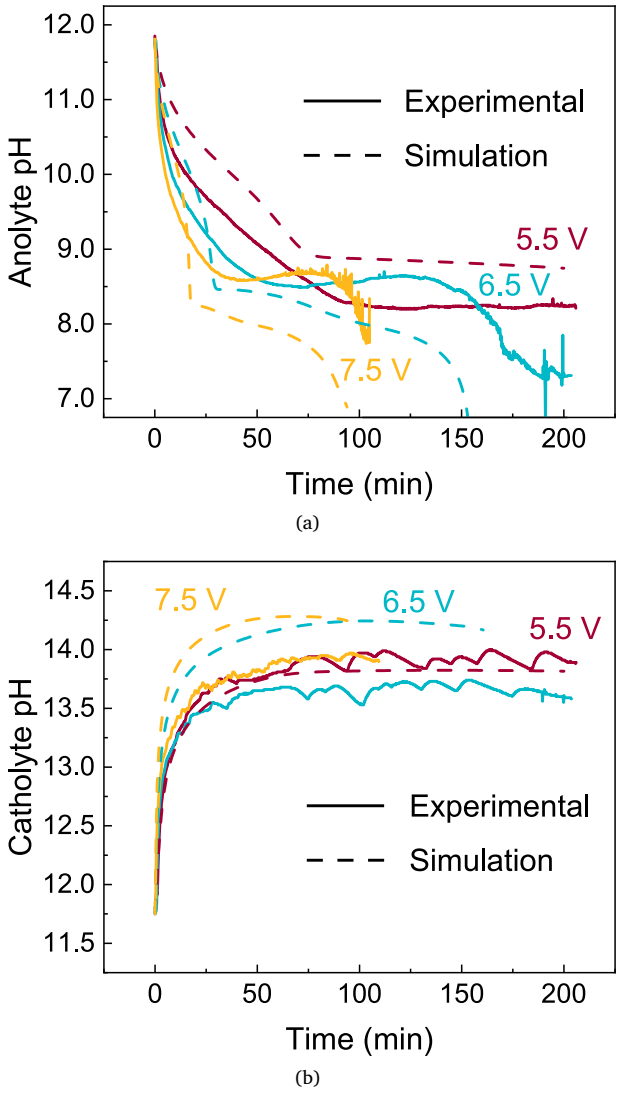

Fig. 6. Comparison between experiments and simulations of the pH of (a) anolyte reservoir and (b) catholyte reservoir beginning at pH 11.75, corresponding to 1 M Na_2CO_3 at 1 bar and 298.15 K. The measurement error of the pH was ±0.02 pH units, but likely increased as the catholyte pH reached the sensor range limit of 14.

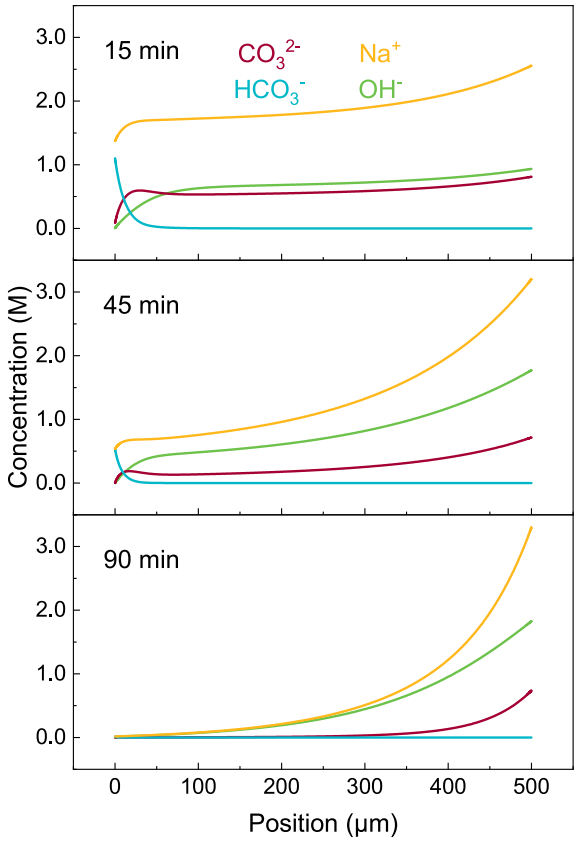

Fig. 7. Plot of the relevant species' concentrations across the separator at different times for the case of 7.5 V cell potential. Simulations were performed at 1 bar and 25 °C, beginning with 1 M Na_2CO_3. The left side at 0 μm represents the anode while the right side at 500 μm represents the cathode. The concentration of HCO_3^- first increases at the anode and then decreases as the dissolved carbon species are slowly removed from the separator. The Supplementary Materials also include short movies of these species' concentrations across the separator over time for the cases of 5.5, 6.5, and 7.5 V cell potential.

Fig. 8a shows the relevant species' concentrations in the anolyte from simulations at 7.5 V. As current continues flowing through the system, the oxygen gas bubbles produced by OER strip away dissolved CO_2 into the gaseous phase as CO_2(g). This removal of aqueous CO_2 from the anolyte and the continued consumption of OH^- at the anode shift the equilibrium of Eq. (9) towards aqueous CO_2 due to Le Chatelier's principle. This then allows further physical gas stripping of CO_2 and further equilibrium shift, thus continuing the cycle. Eventually, all of the dissolved carbon species are fully removed from the anolyte and both the current and pH decrease sharply, as seen in Figs. 4 and 6a, respectively. It should be noted that the simulations without any physical CO_2 stripping do not correctly replicate the current vs time profiles, as HCO_3^- does not equilibrate to CO_2 quickly enough without the active removal of CO_2. The experimental confirmation of this result is discussed in Section 3.4, and a plot of simulation results without CO_2 stripping is shown in Figure S6.

While the anolyte reservoir depletes due to OH^- consumption outpacing transport across the diaphragm, the catholyte reservoir instead concentrates as the produced OH^- cannot transport quickly enough to the anode. Fig. 8b shows the relevant species' concentrations in the catholyte from simulations at 7.5 V. The low concentration of HCO_3^- initially present quickly drops to near zero as the large excess of OH^- produced shifts the equilibrium towards CO_3^{2-}. After the small initial increase, the CO_3^{2-} concentration then decreases due to diffusion and migration towards the anode, while the OH^- concentration steadily rises. As the current drops due to ion depletion at the anode, the uptake of atmospheric CO_2 into the catholyte reservoir combined with a decreasing accumulation of OH^- starts to slightly increase the CO_3^{2-} concentration again. This follows naturally from the equilibrium relationship where a small amount of CO_2 introduced into an alkaline system quickly equilibrates fully to CO_3^{2-}. By examining the final amount of CO_2(g) in the anolyte compared to the starting amounts of CO_3^{2-} and HCO_3^-, it is clear that the anolyte loses a larger amount of dissolved carbon species than was initially present, and that this came from the catholyte.

The simulations for the species' concentrations in each reservoir for 7.5 V and 6.5 V show a similar shape, but at different time scales, with the HCO_3^- also fully depleting near the end of the simulation for 6.5 V. However, the simulation for 5.5 V shows an even slower time scale where the HCO_3^- concentration first increases, but then does not fully decrease to zero within the simulation time of 200 min. The plots of the species' concentrations in the reservoirs for different cell potentials

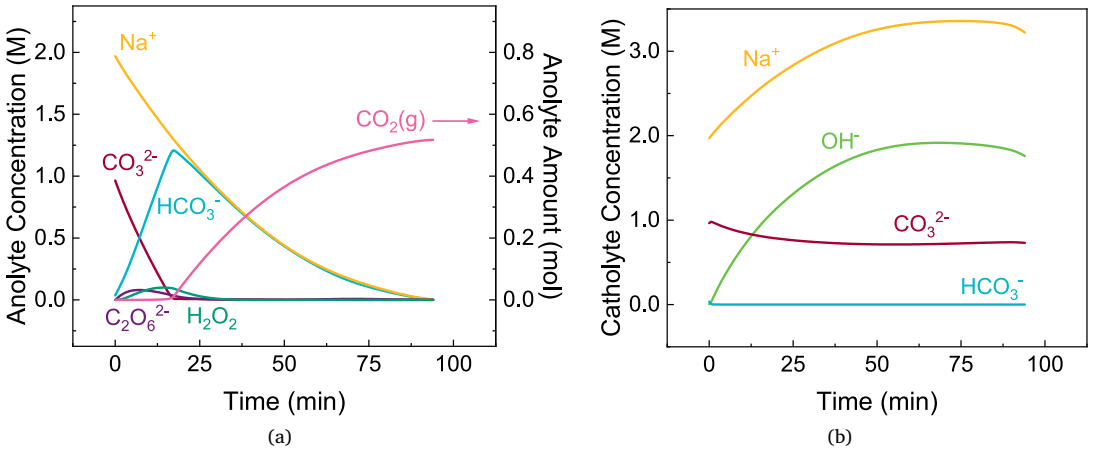

Fig. 8. Simulations of species concentrations in the (a) anolyte reservoir and (b) catholyte reservoir for a cell potential of 7.5 V at 1 bar, 298.15 K, beginning with 1 M Na_2CO_3. The ions depleted in the anolyte are correspondingly accumulated in the catholyte, leading to a large pH gradient across the separator, as seen in Fig. 6. Fig. 8b shows that the CO_3^{2-} concentration in the catholyte never rises past the solubility limit, avoiding salt precipitation.

are shown in Figures S3a-d. The plots of the species' amounts in the reservoirs for all cell potentials are shown in Figures S4a-f.

3.3. H_2O_2 formation

Alongside the depletion of dissolved carbon species, there are anodic reactions involved in the formation of H_2O_2. While there is initially CO_3^{2-} present in the anolyte, the dimerization reaction at the anode surface to form $C_2O_6^{2-}$ shown in Eq. (6) can occur. This $C_2O_6^{2-}$ then reacts with water to form H_2O_2 with a small time delay based on the rate constant of $C_2O_6^{2-}$ decay. The formed H_2O_2 then decays homogeneously and at the anode surface, leading to an exponential decay. The comparison of H_2O_2 concentration in the anolyte in the 7.5 V case can be seen in Fig. 9. The difference between simulation and experimental values could be due to a number of factors, including that the actual kinetic rate constants change as the pH and anolyte composition change over time, which is not accounted for in the simulation. But the qualitative agreement between experimental and simulation results provides secondary evidence for the hypothesis that H_2O_2 is generated through a catalytic cycle involving $C_2O_6^{2-}$, rather than by direct electrochemical generation at the anode surface.

3.4. Gaseous CO_2 evolution

As described in Section 2.2, the evolved gas from the anolyte chamber was passed through a barium solution in order to precipitate dissolved CO_2 as $BaCO_3$. For the case of 7.5 V, Fig. 8a predicts that a total of 0.52 moles of CO_2(g) should be evolved. For complete capture and conversion of this CO_2(g) to $BaCO_3$, this would mean an expected dry precipitate mass of 102.6 g. The experimental mass of dry precipitate measured was 31.9 g. There could be numerous reasons for this large discrepancy, such as insufficient mixing time for the gas bubbles to interact with the barium solution, or not using a large enough molar excess of barium in solution to fully capture all of the CO_2. But this result provides at least a qualitative validation of the significant evolution of gaseous CO_2 during electrolyzer operation. Visually, the barium solution remained relatively clear until the 15 min mark and then started becoming cloudy due to the formation of $BaCO_3$ precipitate. This corresponds with the simulation results for species' concentrations shown in Fig. 8a, where CO_2(g) begins to evolve around the same time. The evolution of CO_2 over time and in significant quantity was also reported by Ma et al. but their setup had an active supply of CO_2. [19]

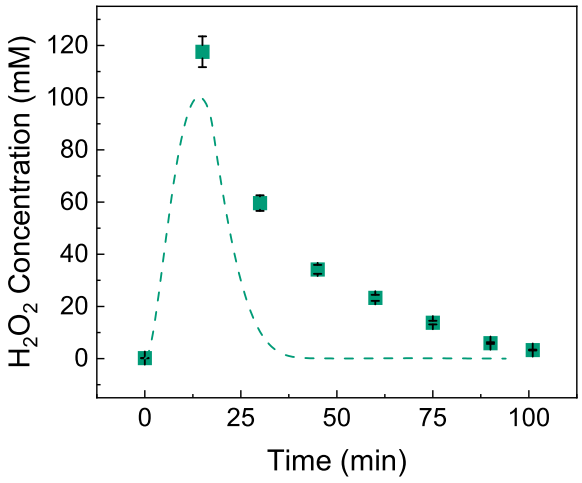

Fig. 9. Plot of experimental vs simulated H_2O_2 concentrations at 7.5 V, showing fairly good agreement in both timescale and magnitude, with error bars based on propagation of uncertainty. The concentration values from the simulation are the sum of HO_2^- and H_2O_2. Experimental measurements are expected to include both species as well, because the measurement procedure involves an acidification step. The experimentally measured H_2O_2 concentration decays more slowly, which could be due to changing decomposition kinetics in the anolyte as the pH decreases over time.

3.5. Considerations for scale-up

From the above results, we see that (bi)carbonate-based electrolyzer systems steadily lose dissolved carbon when pushed to high currents, which could have more implications on the scaled-up system in question beyond the issue of electrolyte depletion. For example, the CO_2 reduction reaction typically involves feeding CO_2 through a gas-diffusion electrode at the cathode side, aiming to convert it to higher value hydrocarbons. The greater ambition of the technology is to upcycle CO_2 emissions to close the carbon cycle, but any unreacted CO_2 at the cathode will become a dissolved carbon species, which will have the tendency to migrate to the anolyte and be stripped away as gaseous CO_2 or precipitate near the cathode [38]. This results in a loss of the CO_2 that ideally would be reacted in order to close the carbon loop. Another case where this transport of carbon species in the system plays a significant role is the formation of anodic H_2O_2. For this reaction, the

electrolyte composition has implications on the generation and stability of H_2O_2 [39,40]. Continually losing dissolved carbon species through this electrolyte depletion mechanism and the resultant pH swing may significantly alter kinetics, in addition to shortening the achievable reaction time.

It may be difficult to find solutions for electrolyte depletion when the use of a rebalancing line is prohibited due to liquid product formation. In-line separation of the liquid product directly following electrolysis would allow for rebalancing [36]. If in-line separation is not possible, sustaining the electrochemical reaction may require injection of alkaline solution to the anolyte. This lowers the concentration of liquid product, but should hopefully keep the carbon species concentration relatively constant, which may help product stability. However, the continual injection of solution to the system cannot be maintained in a fully continuous process. The true solution may rest in switching from porous separators to newer anion exchange membranes that offer superior transport of OH^-, but they also indiscriminately transport negatively charged ions, such as CO_3^{2-} and HCO_3^-, and the operational stability of these new membranes has not yet reached the necessary targets for commercialization [41–43]. Another solution could be operating at sufficiently low current densities such that OH^- transport is sufficiently fast, but this dramatically lowers the overall chemical production rate. Other promising solutions have been researched to prevent dissolved carbon species crossover, such as the use of bipolar membranes, different cationic species such as Cs^+, or even using solid electrolyte between the electrodes, but these solutions introduce additional complications to the scalability and long-term operation of the system and require further study [18,44,45].

4. Conclusion

We show combined experimental and simulation results to understand the dynamics of ion transport and electrolyte depletion in (bi)carbonate-based electrolyzer systems. The equilibrium reactions of (bi)carbonate electrolyte provide a source of OH^- anions that can sustain the anodic reactions, but this results in continual depletion of anolyte species. While the first equilibration of CO_3^{2-} to HCO_3^- occurs readily, the second equilibration of HCO_3^- to CO_2 is assisted by the physical gas stripping from the oxygen produced during OER. There is an overall net flux of dissolved carbon species from catholyte to anolyte, as dissolved CO_3^{2-} and HCO_3^- transport over to the anolyte and equilibrate away to provide more OH^- for the anodic reactions. This work highlights the issue of using (bi)carbonate-based electrolyte, which is that the systems are only viable at lab-scale current densities for lab-scale operational times. Solving this issue for commercialization will require new process flows such as in-line separation of products from the electrolyte or new technologies for the separators such as bipolar membranes or solid electrolyte systems. Future work on this topic could include using new separators, operating at higher temperatures, or changing electrolyte concentrations.

CRediT authorship contribution statement

Sohan A. Phadke: Writing – review & editing, Writing – original draft, Visualization, Methodology, Investigation, Formal analysis, Conceptualization. **J.W. Haverkort:** Writing – review & editing, Supervision, Funding acquisition, Conceptualization. **Wiebren de Jong:** Writing – review & editing, Supervision, Funding acquisition, Conceptualization.

Declaration of competing interest

The authors declare that they have no known competing financial interests or personal relationships that could have appeared to influence the work reported in this paper.

Acknowledgments

This project received funding from the NWO-AES Crossover program under project number 17621 (RELEASE). The authors would like to thank W. L. van der Does for helpful discussions and assistance with the numerical model.

Appendix A. Supplementary data

Supplementary material related to this article can be found online at https://doi.org/10.1016/j.electacta.2026.149379.

Data availability

Data will be made available on request.

References

[1] I.A. Bashmakov, L.J. Nilsson, A. Acquaye, C. Bataille, J.M. Cullen, S. de la Rue du Can, M. Fischedick, Y. Geng, K. Tanaka, Industry. IPCC, 2022: Climate Change 2022: Mitigation of Climate Change, in: Contribution of Working Group III to the Sixth Assessment Report of the Intergovernmental Panel on Climate Change, 2022, http://dx.doi.org/10.1017/9781009157926.013.

[2] B. Chang, H. Pang, F. Raziq, S. Wang, K.-W. Huang, J. Ye, H. Zhang, Electrochemical reduction of carbon dioxide to multicarbon (C_{2+}) products: challenges and perspectives, Energy Environ. Sci. 16 (2023) 4714–4758, http://dx.doi.org/10.1039/d3ee00964e.

[3] V. Viswanathan, H.A. Hansen, J.K. Nørskov, Selective Electrochemical Generation of Hydrogen Peroxide from Water Oxidation, J. Phys. Chem. Lett. 6 (2015) 4224–4228, http://dx.doi.org/10.1021/acs.jpclett.5b02178.

[4] L. Li, R.P. Antony, C. Santana Santos, N. Limani, S. Dieckhöfer, W. Schuhmann, Anodic H_2O_2 Generation in Carbonate-Based Electrolytes - Mechanistic Insight from Scanning Electrochemical Microscopy, Angew. Chem. Int. Ed. 63 (2024) e202406543, http://dx.doi.org/10.1002/anie.202406543.

[5] I.A.E. Burgers, T.M.J. Nijssen, S. Feith, R. Kortlever, E.L.V. Goetheer, Direct Air Capture with Integrated Electrochemical Conversion through Combined Solid and Liquid Sorbents, ACS Sustain. Chem. Eng. 14 (2026) 3826–3833, http://dx.doi.org/10.1021/acssuschemeng.5c07683.

[6] G. Lee, A.S. Rasouli, B.-H. Lee, J. Zhang, D.H. Won, Y.C. Xiao, J.P. Edwards, M.G. Lee, E.D. Jung, F. Arabyarmohammadi, H. Liu, I. Grigioni, J. Abed, T. Alkayyali, S. Liu, K. Xie, R.K. Miao, S. Park, R. Dorakhan, Y. Zhao, C.P. O'Brien, Z. Chen, D. Sinton, E. Sargent, CO_2 electroreduction to multicarbon products from carbonate capture liquid, Joule 7 (2023) 1277–1288, http://dx.doi.org/10.1016/j.joule.2023.05.003.

[7] H. Song, C.A. Fernández, A. Venkataraman, V.D. Brandão, S.S. Dhingra, S.S. Arora, S.S. Bhargava, C.M. Villa, C. Sievers, S. Nair, M.C. Hatzell, Ethylene Production from Carbonate Using a Bipolar Membrane Electrolysis System, ACS Appl. Energy Mater. 7 (2024) 1224–1233, http://dx.doi.org/10.1021/acsaem.3c02758.

[8] D. Pangotra, L.-I. Csepei, A. Roth, C. Ponce de Léon, V. Sieber, L. Vieira, Anodic production of hydrogen peroxide using commercial carbon materials, Appl. Catal. B: Environ. 303 (2022) 120848, http://dx.doi.org/10.1016/j.apcatb.2021.120848.

[9] J.A. Dean, Lange's Handbook of Chemistry, Fifteen ed., McGraw-Hill, 1999.

[10] H. Ito, N. Kawaguchi, S. Someya, T. Munakata, N. Miyazaki, M. Ishida, N. Akihiro, Experimental investigation of electrolytic solution for anion exchange membrane water electrolysis, Int. J. Hydrog. Energy 43 (2018) 17030–17039, http://dx.doi.org/10.1016/j.ijhydene.2018.07.143.

[11] J.W. Haverkort, H. Rajaei, Electro-osmotic flow and the limiting current in alkaline water electrolysis, J. Power Sources Adv. 6 (2020) 100034, http://dx.doi.org/10.1016/j.powera.2020.100034.

[12] G.O. Larrazábal, P. Strøm-Hansen, J.P. Heli, K. Zeiter, K.T. Therkildsen, I. Chorkendorff, B. Seger, Analysis of Mass Flows and Membrane Cross-over in CO_2 Reduction at High Current Densities in an MEA-Type Electrolyzer, ACS Appl. Mater. Interfaces 11 (2019) 41281–41288, http://dx.doi.org/10.1021/acsami.9b13081.

[13] P. Mardle, S. Cassegrain, F. Habibzadeh, Z. Shi, S. Holdcroft, Carbonate ion crossover in zero-gap, KOH anolyte CO_2 electrolysis, J. Phys. Chem. C 125 (2021) 25446–25454, http://dx.doi.org/10.1021/acs.jpcc.1c08430.

[14] R. Lira Garcia Barros, J.T. Kraakman, C. Sebregts, J. van der Schaaf, M.T. de Groot, Impact of an electrode-diaphragm gap on diffusive hydrogen crossover in alkaline water electrolysis, Int. J. Hydrog. Energy 49 (2024) 886–896, http://dx.doi.org/10.1016/j.ijhydene.2023.09.280.

[15] M. Ma, S. Kim, I. Chorkendorff, B. Seger, Role of ion-selective membranes in the carbon balance for CO_2 electroreduction via gas diffusion electrode reactor designs, Chem. Sci. 11 (2020) 8854–8861, http://dx.doi.org/10.1039/D0SC03047C.

[16] G.O. Larrazábal, M. Ma, B. Seger, A Comprehensive Approach to Investigate CO_2 Reduction Electrocatalysts at High Current Densities, Accounts Mater. Res. 2 (2021) 220–229, http://dx.doi.org/10.1021/accountsmr.1c00004.

[17] M. Ramdin, O.A. Moultos, L.J.P. van den Broeke, P. Gonugunta, P. Taheri, T.J.H. Vlugt, Carbonation in low-temperature CO_2 electrolyzers: Causes, consequences and solutions, Ind. Chem. Eng. Res. 62 (2023) 6843–6864, http://dx.doi.org/10.1021/acs.iecr.3c00118.

[18] Y.C. Li, Z. Yan, J. Hitt, R. Wycisk, P.N. Pintauro, T.E. Mallouk, Bipolar Membranes Inhibit Product Crossover in CO_2 Electrolysis Cells, Adv. Sustain. Syst. 2 (2018) 1700187, http://dx.doi.org/10.1002/adsu.201700187.

[19] M. Ma, E.L. Clark, K.T. Therkildsen, S. Dalsgaard, I. Chorkendorff, B. Seger, Insights into the Carbon Balance for CO_2 Electroreduction on Cu using Gas Diffusion Electrode Reactor Designs, Energy & Environ. Sci. 13 (2020) 977–985, http://dx.doi.org/10.1039/D0EE00047G.

[20] A.B. Moss, S. Garg, M. Mirolo, C.A. Giron Rodriguez, R. Ilvonen, I. Chorkendorff, J. Drnec, B. Seger, In operando investigations of oscillatory water and carbonate effects in MEA-based CO_2 electrolysis devices, Joule 7 (2023) 350–365, http://dx.doi.org/10.1016/j.joule.2023.01.013.

[21] Q. Xu, S. Liu, F. Longhin, G. Kastlunger, I. Chorkendorff, B. Seger, Impact of Anodic Oxidation Reactions in the Performance Evaluation of High-Rate CO_2/CO Electrolysis, Adv. Mater. 36 (2023) 2306741, http://dx.doi.org/10.1002/adma.202306741.

[22] A. Raya-Imbernón, A.A. Samu, S. Barwe, G. Cusati, T. Fődi, B.M. Hepp, C. Janáky, Renewable syngas generation via low-temperature electrolysis: Opportunities and challenges, ACS Energy Lett. 9 (2024) 288–297, http://dx.doi.org/10.1021/acsenergylett.3c02446.

[23] V.D. Brandaão, H. Song, A. Venkataraman, Y. Fishler, S.S. Arora, S.S. Bhargava, C. Villa, A. Holewinski, S. Nair, M.C. Hatzell, C. Sievers, Temperature Effects on the Surface CO Population during CO_2 Electroreduction over Copper, ACS Catal. 15 (2025) 8979–8990, http://dx.doi.org/10.1021/acscatal.5c01173.

[24] J. Li, H. Zhang, C. Luo, D. Cheng, W. Xu, M. Lin, Non-isothermal CO_2 electrolysis enables simultaneous enhanced electrochemical and anti-precipitation performance, Nat. Commun. 16 (2025) 4181, http://dx.doi.org/10.1038/s41467-025-59604-.

[25] C.C. Lin, F.R. Smith, N. Ichikawa, T. Baba, M. Itow, Decomposition of hydrogen peroxide in aqueous solutions at elevated temperatures, Int. J. Chem. Kinet. 23 (1991) 971–987, http://dx.doi.org/10.1002/kin.550231103.

[26] J.W. Haverkort, Modeling and experiments of binary electrolytes in the presence of diffusion,migration, and electro-osmotic flow, Phys. Rev. Appl. 14 (2020) http://dx.doi.org/10.1103/PhysRevApplied.14.044047.

[27] P.M. v. d. Wiel, L.J.J. Janssen, J.G. Hoogland, Electrolysis of a carbonate-borate solution with a platinum anode-I. Current efficiency at perborate concentration of zero, Electrochim. Acta 16 (1971) 1217–1226, http://dx.doi.org/10.1016/0013-4686(71)85110-1.

[28] A. Ziogas, J. Belda, H.-J. Kost, J. Magomajew, R.A. Sperling, P. Wernig, Peroxodicarbonate: Electrosynthesis and first directions to green industrial applications, Curr. Res. Green Sustain. Chem. 5 (2022) 100341, http://dx.doi.org/10.1016/j.crgsc.2022.100341.

[29] T. Rücker, N. Schupp, F. Sprang, T. Horsten, B. Wittgens, S.R. Waldvogel, Peroxodicarbonate – a renaissance of an electrochemically generated green oxidizer, Chem. Commun. 60 (2024) 7136–7147, http://dx.doi.org/10.1039/d4cc02501f.

[30] D. Pangotra, L.-I. Csepei, A. Roth, V. Sieber, L. Vieira, Anodic generation of hydrogen peroxide in continuous flow, Green Chem. 24 (2022) 7931–7940, http://dx.doi.org/10.1039/d2gc02575b.

[31] T.M. Gill, X. Zheng, Comparing Methods for Quantifying Electrochemically Accumulated H_2O_2, Chem. Mater. 32 (2020) 6285–6294, http://dx.doi.org/10.1021/acs.chemmater.0c02010.

[32] L.-C. Weng, A.T. Bell, A.Z. Weber, Modeling gas-diffusion electrodes for CO_2 reduction, Phys. Chem. Chem. Phys. 20 (2018) 16973–16984, http://dx.doi.org/10.1039/c8cp01319e.

[33] J.W. Blake, J.T. Padding, J.W. Haverkort, Analytical modelling of CO_2 reduction in gas-diffusion electrode catalyst layers, Electrochim. Acta 393 (2021) 138987, http://dx.doi.org/10.1016/j.electacta.2021.138987.

[34] R.E. Vos, M.T.M. Koper, Nickel as electrocatalyst for CO_2 reduction: Effect of temperature, potential, partial pressure, and electrolyte composition, ACS Catal. 14 (2024) 4432–4440, http://dx.doi.org/10.1021/acscatal.4c00009.

[35] M.A. Nazir, M.M. Abou-Krisha, S. Afzal, S. Ullah, T. Najam, S. Bashir, E.A. Abdelrahman, S.S.A. Shah, Ni-based electrocatalysts for carbon dioxide reduction reaction: A critical review on recent advances and industrial perspectives, Sep. Purif. Technol. 397 (2026) 138086, http://dx.doi.org/10.1016/j.seppur.2026.138086.

[36] M. Ramdin, B. De Mot, A.R.T. Morrison, T. Breugelmans, L.J.P. van den Broeke, J.P.M. Trusler, R. Kortlever, W. de Jong, O.A. Moultos, P. Xiao, P.A. Webley, T.J.H. Vlugt, Electroreduction of CO_2/CO to C_2 products: Process modeling, downstream separation, system integration, and economic analysis, Ind. Eng. Chem. Res. 60 (2021) 17862–17880, http://dx.doi.org/10.1021/acs.iecr.1c03592.

[37] H. Zhong, K. Fujii, Y. Nakano, F. Jin, Effect of CO_2 Bubbling into Aqueous Solutions Used for Electrochemical Reduction of CO_2 for Energy Conversion and Storage, J. Phys. Chem. C 119 (2014) 55–61, http://dx.doi.org/10.1021/jp509043h.

[38] J.A. Rabinowitz, M.W. Kanan, The future of low-temperature carbon dioxide electrolysis depends on solving one basic problem, Nat. Commun. 11 (2020) http://dx.doi.org/10.1038/s41467-020-19135-8.

[39] T.M. Gill, L. Vallez, X. Zheng, The Role of Bicarbonate-Based Electrolytes in H_2O_2 Production through Two-Electron Water Oxidation, ACS Energy Lett. 6 (2021) 2854–2862, http://dx.doi.org/10.1021/acsenergylett.1c01264.

[40] H.H.B. Lee, A.-H. Park, C. Oloman, Stability of Hydrogen Peroxide in Sodium Carbonate Solutions, Tappi J. 83 (2000) 1–9.

[41] D. Henkensmeier, W. Cho, P. Jannasch, J. Stojadinovic, Q. Li, D. Aili, J.O. Jensen, Separators and Membranes for Advanced Alkaline Water Electrolysis, Chem. Rev. 124 (2024) 6393–6443, http://dx.doi.org/10.1021/acs.chemrev.3c00694.

[42] L. Ge, H. Rabiee, M. Li, S. Subramanian, Y. Zheng, J.H. Lee, T. Burdyny, H. Wang, Electrochemical CO_2 reduction in membrane-electrode assemblies, Chem 8 (2022) 663–692, http://dx.doi.org/10.1016/j.chempr.2021.12.002.

[43] J. Herranz, A. Pătru, E. Fabbri, T.J. Schmidt, Co-electrolysis of CO_2 and H_2O: From electrode reactions to cell-level development, Curr. Opin. Electrochem. 23 (2020) 89–95, http://dx.doi.org/10.1016/j.coelec.2020.05.004.

[44] B. Pan, J. Fan, J. Zhang, Y. Luo, C. Shen, C. Wang, Y. Wang, Y. Li, Close to 90% Single-Pass Conversion Efficiency for CO_2 Electroreduction in an Acid-Fed Membrane Electrode Assembly, ACS Energy Lett. 7 (2022) 4224–4231, http://dx.doi.org/10.1021/acsenergylett.2c02292.

[45] Y. Xu, R.K. Miao, J.P. Edwards, S. Liu, C.P. O'Brien, C.M. Gabardo, M. Fan, J.E. Huang, A. Robb, E.H. Sargent, D. Sinton, A microchanneled solid electrolyte for carbon-efficient CO_2 electrolysis, Joule 6 (2022) 1333–1343, http://dx.doi.org/10.1016/j.joule.2022.04.023.